NMR IN BIOMEDICINE
NMR Biomed. 2008; **21**: 888–898
Published online 23 June 2008 in Wiley InterScience
(www.interscience.wiley.com) DOI:10.1002/nbm.1277

Three-dimensional water diffusion in impermeable cylindrical tubes: theory versus experiments

Liat Avram,[1] Evren Özarslan,[2] Yaniv Assaf,[3,4] Amnon Bar-Shir,[1] Yoram Cohen[1] and Peter J. Basser[2]*

[1]School of Chemistry, The Raymond and Beverly Sackler Faculty of Exact Sciences, Tel-Aviv University, Tel-Aviv, Israel
[2]Section on Tissue Biophysics and Biomimetics, NICHD, NIH, Bethesda, MD, USA
[3]Department of Neurobiochemistry, Tel Aviv University, Tel-Aviv, Israel
[4]Functional Brain Imaging Unit, Sourasky Medical Center, Tel-Aviv, Israel

Received 19 December 2007; Revised 7 March 2008; Accepted 10 March 2008

ABSTRACT: Characterizing diffusion of gases and liquids within pores is important in understanding numerous transport processes and affects a wide range of practical applications. Previous measurements of the pulsed gradient stimulated echo (PGSTE) signal attenuation, $E(\mathbf{q})$, of water within nerves and impermeable cylindrical microcapillary tubes showed it to be exquisitely sensitive to the orientation of the applied wave vector, $\mathbf{q}$, with respect to the tube axis in the high-$\mathbf{q}$ regime. Here, we provide a simple three-dimensional model to explain this angular dependence by decomposing the average propagator, which describes the net displacement of water molecules, into components parallel and perpendicular to the tube wall, in which axial diffusion is free and radial diffusion is restricted. The model faithfully predicts the experimental data, not only the observed diffraction peaks in $E(\mathbf{q})$ when the diffusion gradients are approximately normal to the tube wall, but their sudden disappearance when the gradient orientation possesses a small axial component. The model also successfully predicts the dependence of $E(\mathbf{q})$ on gradient pulse duration and on gradient strength as well as tube inner diameter. To account for the deviation from the narrow pulse approximation in the PGSTE sequence, we use Callaghan's matrix operator framework, which this study validates experimentally for the first time. We also show how to combine average propagators derived for classical one-dimensional and two-dimensional models of restricted diffusion (e.g. between plates, within cylinders) to construct composite three-dimensional models of diffusion in complex media containing pores (e.g. rectangular prisms and/or capped cylinders) having a distribution of orientations, sizes, and aspect ratios. This three-dimensional modeling framework should aid in describing diffusion in numerous biological systems and in a myriad of materials sciences applications. Copyright © 2008 John Wiley & Sons, Ltd.

KEYWORDS: *q*-space; diffusion; restricted; capillary; tube; orientation; diameter

INTRODUCTION

The microstructure and morphology of porous media determine their material behavior and transport properties. Thus, characterizing these features of pores is critical to many areas of materials science and technology. For example, in geology and geophysics, information about pore architecture and microstructure of rocks, such as their tortuosity and surface-to-volume ratio, is used to describe their natural history and to determine the ease of oil extraction from them. In polymer physics, macromolecular-sized cylindrical 'tubes' through which long-chain polymers reptate (1) can be viewed as pores. Knowledge of the displacement distribution of monomers on the backbone of long-chain polymers, as well as the shape of this reptation tube, is useful in understanding polymer mobility (2). Finally, in materials engineering and biotechnology applications, morphological and microstructural features of porous materials determine transport of charge, mass, momentum, and heat, and are thus critical properties in applications ranging from catalysis (3) to water purification to tissue engineering (4).

The function of biological tissue is also affected by its microstructure and morphology; increasing evidence indicates that many tissues, such as nerve axons, can be treated as porous media. King *et al*. (5,6) used one-dimensional *q*-space NMR to measure the average propagator in neuronal tissue. The Cohen group later suggested the use of *q*-space diffusion MRI to study white matter structure and pathology (7–11). Other soft tissues exhibiting features of porous media include skeletal muscle (12) and cardiac myocytes (13). Air spaces within bronchi, bronchioles, and alveoli in the lung can be viewed as interconnected pores (14) of an open-cell foam, the microstructure of which may be altered during

**Correspondence to:* P. J. Basser, NIH, 13 South Drive, MSC 5772, Building 13, Room 3W16, Bethesda, MD 20892-5772, USA.
E-mail: pjbasser@helix.nih.gov

Abbreviations used: 3D, three-dimensional; CHARMED, composite hindered and restricted model of diffusion; ID, inner diameter; DTI, diffusion tensor MRI; PGSTE, pulsed gradient stimulated echo.

development and in disease. Plant cells, which have cellulose membranes that provide an impermeable barrier to water transport, offer another example of biological media in which restricted diffusion within pores is observed (15). Restricted diffusion in blood cells (16) and cellular systems (17) has also been studied.

NMR and MRI methods are playing an increasingly important role in materials sciences, revealing microstructural and architectural features, particularly in optically turbid or opaque porous media, from the macromolecular to macroscopic length scales. The most widely used and powerful MR methods for measuring material morphology, particularly in porous media, use diffusion-weighted MR signals, in particular, q-space NMR (18) and q-space MRI (19). These methods can provide an estimate of the three-dimensional (3D) displacement distribution of spin-labeled molecules (such as protons in water) without the need to invoke a model of the material's morphology or microstructure where molecules are diffusing and/or flowing – information that typically is not known *a priori*.

The q-space MR methods are particularly powerful when the material has impermeable or semi-permeable inclusions or pores, in which case spin-labeled molecules are confined within these spaces. Then, q-space MR methods yield useful morphological information about these pores, such as their dimensions, from the observed diffraction peaks observed in the MR signal profile (20). Other properties of interest that can be gleaned from these data include tortuosity (21), surface-to-volume ratio (22), degree of pore interconnectivity (18), and pore size distribution (23). With q-space MR, it is also possible to probe an enormous range of pore sizes [e.g. see Fig. 5 in Ref. (24)], from meters (e.g. using hyperpolarized noble gases in the lung) to nanometers [e.g. using protons residing on long-chain polymers (25)].

Currently, it is difficult to use MR methods to explore the microstructure and morphology of tissues because of the dearth of general 3D diffusion models for interpreting 3D q-space MRI data. Except for the work of Boss and Stejskal (26), Söderman and Jönsson (27), and, most recently, Assaf *et al*. (28,29), q-space MR methods developed to examine the structure or morphology of ordered porous media are one-dimensional or two-dimensional, requiring that the sample be oriented with the magnetic field gradient applied perpendicular to the restricting boundary (18,30–34). (Boss and Stejskal rotated their specimen within the NMR magnet rather than fix its position and change the orientation of the diffusion gradients.) However, in many practical applications, e.g. in opaque or optically turbid media, the orientation of the material's principal axes with respect to the laboratory coordinate frame is generally not known *a priori*. Moreover, if the material is both anisotropic and heterogeneous, as most biological tissues are, then the orientation of the principal or symmetry axes generally varies from voxel to voxel. Such is the case in white matter in the brain, the principal axes of which can be determined by diffusion tensor MRI (DTI) (35,36).

In neuroscience and neurological applications, one may wish to measure microstructure and anatomical features of nerve axon bundles (fascicles) in the peripheral and central nervous systems. These include the local fiber orientation, the mean inner diameter (ID) of a pack of axons, the total intra-axonal volume, the extra-axonal volume, and the axonal volume fraction. Although DTI provides information about tissue microstructure *in vivo*, such as the orientation of coherently organized nerve fibers (35), it does not provide a measurement of these other microstructural quantities of interest.

Thus, it was necessary to develop a tractable 3D framework for treating restricted diffusion in ordered porous media, particularly ordered packs of restricted cylinders. To address this problem, we recently proposed a 3D model that relates the diffusion-weighted MR signal measured in a q-space experiment to the displacement distribution of spin-labeled molecules within a cylindrical pack of impermeable tubes. This composite hindered and restricted model of diffusion (CHARMED) MR framework explicitly accounts for the pack's pore geometry and its orientation with respect to the laboratory coordinate frame (28,29). In CHARMED MR, the mean tube diameter, the tubes' orientation with respect to the laboratory coordinate system, the diffusivity of water within them, and the volume fraction of tubes are all statistically estimated from 3D q-space MR data. To account for the variation in nerve fiber bundle directions in the imaging volume, we developed CHARMED MRI, which combines the CHARMED NMR experiment with MRI sequences for spatial localization (28,29). Using CHARMED MRI, we can estimate these microstructural features on a voxel-by-voxel basis.

The ansatz that makes CHARMED mathematically tractable is the same one invoked here – that random displacements along the tube's axis and random displacements perpendicular to it (i.e. normal to the tube wall) are assumed to be statistically independent. We showed that this assumption simplifies the form of the total average propagator, allowing us to express it as the product of average propagators describing motion along these orthogonal directions. This decomposition was shown to imply that the total signal attenuation could be factored as the product of the signal attenuations associated with displacements parallel and perpendicular to the tube axis. Thus, we are able to construct a full 3D model of diffusion within the tube by combining classical solutions of the diffusion equation [e.g. see Ref. (37)] appropriate for motion along the axial and radial directions. This is the same approach that we adopt here to describe diffusion within a pack of impermeable fused silica microcapillaries.

The second difficulty in applying q-space MRI methods in a biological or clinical setting is the inability to satisfy the 'narrow pulse' approximation in pulse field gradient experiments used to acquire q-space MR data. If

DOI: 10.1002/nbm

this assumption is not satisfied, the Fourier transform relationship between the signal attenuation and the average propagator cannot be used directly (30,38).

For example, one difficulty in interpreting CHARMED MRI data has been to relate the measured signal attenuation to the diameter of the axon when the diffusion-weighted MR sequence incorporates 'fat' diffusion gradient pulses. As this approach is generally implemented on a clinical scanner where peak gradient strengths are limited and slew rates are low, conditions invariably arise in which the narrow pulse approximation is clearly violated. To address this problem, we propose testing the validity and robustness of Callaghan's matrix operator framework in relating the MR signal attenuation to experimental variables such as tube diameter and pulse sequence parameters.

One goal of this paper is to compare new model predictions using the simplifying assumption of statistical independence described above with previously published experimental diffusion MR data (39). In particular, we try to explain the remarkable experimental finding, previously reported by Avram *et al*. (39,40), of a strong dependence of the diffusion-weighted MR signal, $E(\mathbf{q})$, on the magnetic field gradient orientation in a cylindrical pack of water-filled tubes. In addition, we explore the dependence of $E(\mathbf{q})$ on tube diameter as well as on pulsed gradient stimulated echo (PGSTE) sequence parameters, such as the diffusion pulse width. This allows us to assess the adequacy of the 'narrow pulse' approximation, and, in cases where it clearly does not apply, to test Callaghan's matrix operator method for treating pulse gradient diffusion sequences with 'fat pulses' using a well-defined model system. Finally, we show how to use our modeling framework to construct numerical 'phantoms' consisting of packs of tubes with different distributions of inner diameters and tube orientations.

RESTRICTED DIFFUSION IN AN ORIENTED PACK OF IMPERMEABLE TUBES

The NMR experiment used here to probe material microstructure is the PGSTE sequence (41), depicted in Fig. 1a. Following the first and last 90° radiofrequency pulses are two pulsed magnetic field gradients (the pulse duration of which is δ, and temporal separation of which is Δ), which sensitize the NMR echo amplitude to the effects of random motion (42–44).

For this experiment, there is a well-known 3D Fourier transform relationship between the NMR signal attenuation, $E(\mathbf{q}, \Delta)$, and the displacement distribution (i.e. embodied by the 'average propagator'), $\overline{P}(\mathbf{R}, \Delta)$ (18,38,45):

$$E(\mathbf{q},\Delta) = \iiint \overline{P}(\mathbf{R},\Delta)\, e^{2\pi i\, \mathbf{q}\cdot\mathbf{R}}\, d\mathbf{R} \quad \textit{where} \quad \mathbf{q} = \frac{1}{2\pi}\gamma\,\mathbf{g}\delta \tag{1}$$

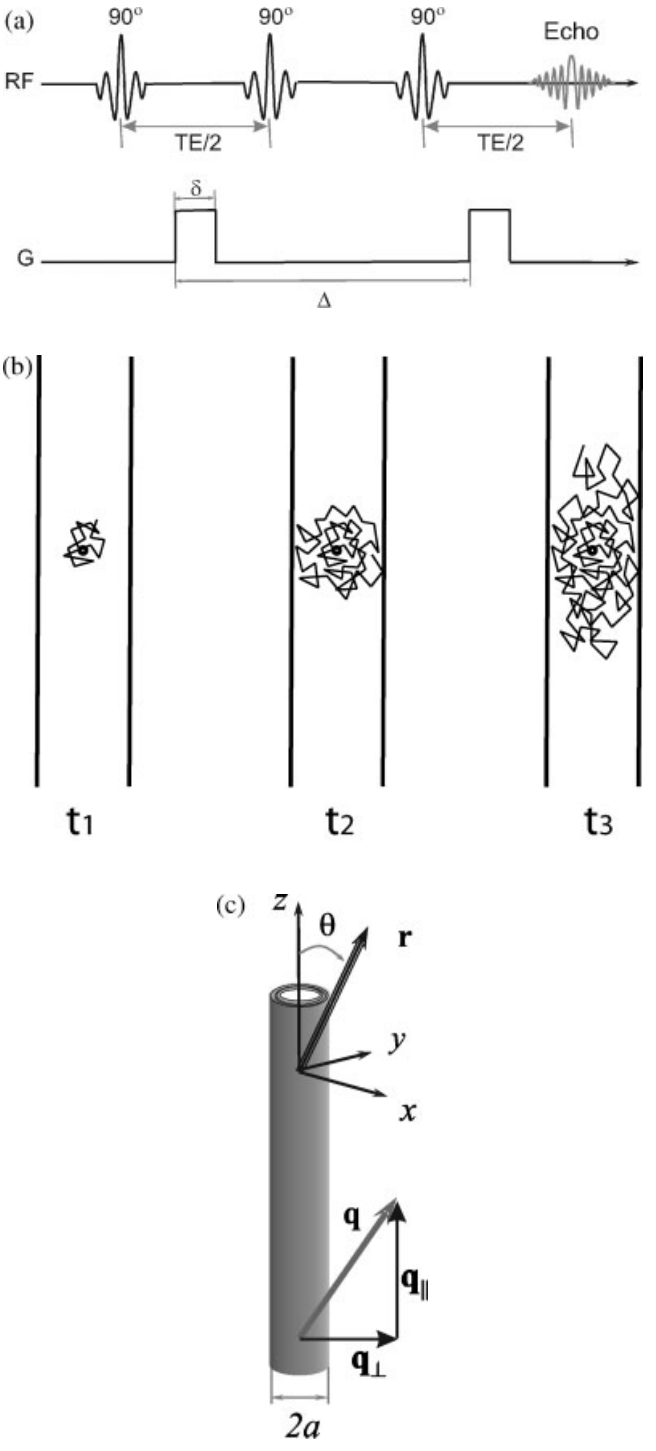

Figure 1. (a) PGSTE sequence with gradient strength, G, pulse duration, δ, gradient pulse separation, Δ, and echo time, TE. (b) Cartoon of a particle undergoing diffusion in a domain that is restricted along one direction and free along the other. Here random displacements are uncoupled in these two orthogonal directions. A random walk is depicted for three subsequent time points, t_1, t_2, and t_3. (c) A pack of impermeable tubes oriented parallel to the z axis in the laboratory coordinate system. Shown are the tube axis, the components of the q vector, $\mathbf{q}$, parallel and perpendicular to the tube axis, $\mathbf{q}_{//}$ and $\mathbf{q}_{\perp}$, respectively, the tube radius, a, and the azimuthal angle, θ.

DOI: 10.1002/nbm

R is the net displacement vector for a diffusing spin, γ is the proton gyromagnetic ratio, **g** is the applied diffusion gradient vector, and **q** is the wave vector that determines the diffusion length scale being probed.

The solution to the diffusion equation in impermeable cylinders and sheets (18,30,46–50) factors into products of terms that depend on the 'natural' coordinates associated with the bounding geometry (47). This appears to be an intrinsic property that justifies the use of the method of separation of variables to solve the governing set of parabolic partial differential equations. In these systems, displacements perpendicular to restricting boundaries are uncoupled from displacements parallel to them. Figure 1b illustrates this in a cartoon of the random displacements of a diffusing particle within a restricted domain at increasing diffusion times. This point is explained in detail in Appendix D of Ref. (29). We showed previously that this condition results in the decoupling of the average propagators associated with motion parallel and perpendicular to the restricting boundary (29):

$$\overline{P}(\mathbf{R},\Delta) = \overline{P}_{\perp}(\mathbf{R}_{\perp},\Delta)\,\overline{P}_{//}(\mathbf{R}_{//},\Delta) \qquad (2)$$

where $\overline{P}_{//}(\mathbf{R}_{//},\Delta)$ and $\overline{P}_{\perp}(\mathbf{R}_{\perp},\Delta)$ are the average propagators for displacements in the parallel and perpendicular directions, respectively. Eqn (2) uses the fact that we can decompose the net displacement vector, **R**, into components or projections parallel and perpendicular to the tube's axis, i.e. $\mathbf{R} = \mathbf{R}_{\perp} + \mathbf{R}_{//}$.

We demonstrated in Appendix A of Assaf *et al*. (29) that, if we decompose any **q** vector in the laboratory coordinate frame into components parallel and perpendicular to the tube's axis, i.e. $\mathbf{q} = \mathbf{q}_{\perp} + \mathbf{q}_{//}$ (see Fig. 1c), then eqns (1) and (2) imply

$$E(\mathbf{q},\Delta) = E_{\perp}(\mathbf{q}_{\perp},\Delta)\,E_{//}(\mathbf{q}_{//},\Delta) \qquad (3)$$

where the MR signals due to random motions projected along the perpendicular and parallel directions, $E_{\perp}(\mathbf{q}_{\perp},\Delta)$and $E_{//}(\mathbf{q}_{//},\Delta)$, respectively, are given by:

$$E_{\perp}(\mathbf{q}_{\perp}) = \iint \overline{P}_{\perp}(\mathbf{R}_{\perp},\Delta)\,e^{2\pi i\mathbf{q}_{\perp}\,\mathbf{R}_{\perp}}\,d\mathbf{R}_{\perp} \quad \text{and}$$
$$E_{//}(\mathbf{q}_{//}) = \int \overline{P}_{//}(\mathbf{R}_{//},\Delta)\,e^{2\pi i\mathbf{q}_{//}\,\mathbf{R}_{//}}\,d\mathbf{R}_{//} \qquad (4)$$

(The double integral indicates that we perform the integration over the tube's cross-section, whereas the single integral is performed along the tube's axis.) Thus, statistical independence of average propagators (eqn 2) along the axial and radial directions of the tube implies the finding in eqn (3) that $E(\mathbf{q},\Delta)$ can be decomposed into the *product* of MR signal attenuations arising from net displacements viewed along directions parallel and perpendicular to the tube's axis, as defined in eqn (4).

For displacements parallel to the axis of an infinite tube, we assume a one-dimensional model of free diffusion. In this case, $E_{//}(\mathbf{q}_{//})$ in eqn (4) is described by the Stejskal–Tanner equation (44):

$$E_{//}(\mathbf{q}_{//}) = e^{-4\pi^2|\mathbf{q}_{//}|^2 D_{//}\left(\Delta-\frac{\delta}{3}\right)} \qquad (5)$$

where $D_{//}$ is the diffusion coefficient of the medium within the tube along the axial direction. (We allow for the possibility that the medium filling the tube is hindered and anisotropic so that the diffusivity parallel and perpendicular to the tube's axis may be different. If the tube is filled with a simple liquid such as water, then $D_{//}$ will be its isotropic diffusion coefficient.) This expression applies for all admissible diffusion times and pulse durations.

Unfortunately, no such simple and general analytical expression exists for the signal attenuation arising from displacements perpendicular to the tube wall, $E_{\perp}(\mathbf{q}_{\perp},\Delta)$. In the limit in which the narrow pulse approximation holds (i.e. $\delta \approx 0$ and $\delta << \Delta$), one can use an expression for $E_{\perp}(\mathbf{q}_{\perp},\Delta)$ proposed by Callaghan (51). In the opposite limit in which a constant diffusion gradient is applied throughout the PGSTE experiment, (i.e. $\delta = \Delta$), $E_{\perp}(\mathbf{q}_{\perp},\Delta)$ can be described by an expression proposed by Neuman (49). In the intermediate regimen in which gradient pulses are 'fat' (i.e. $0 << \delta \leq \Delta$), van Gelderen *et al*. (52) proposed an expression relating pulse sequence parameters to $E_{\perp}(\mathbf{q}_{\perp},\Delta)$. However, the derivations in Refs. (49) and (52) are based on the Gaussian phase approximation, and cannot predict 'diffraction peaks,' such as the ones described below. None of these formulae strictly applies to the experiments performed here, nor could any of them be used over the large range of pulse gradient durations we use here or are typically encountered experimentally.

An alternative to using these analytical models is to use the matrix operator formalism developed by Callaghan (53,54) and adapted to rectangular, cylindrical, and spherical pores with finite wall relaxivity by Codd and Callaghan (50). This approach, based on an idea originally proposed by Caprihan *et al*. (55), breaks up finite width or 'fat' diffusion gradient pulses into a train of narrow pulses, each followed by a brief magnetization evolution period. Using this numerical framework, it is possible to predict $E_{\perp}(\mathbf{q}_{\perp},\Delta)$ in tubes, cylinders, or spheres from PGSTE sequences. One open issue with this approach, however, is that, although it has been tested extensively using Monte Carlo simulations, it has never been validated experimentally using real MR data in well-defined model systems.

METHODS

NMR diffusion experiments were performed on a bundle of fused silica tubes packed into NMR tubes so that the axis of the tubes was kept fixed in the laboratory frame and aligned with the z or main axis of the main magnetic field.

DOI: 10.1002/nbm

Spools of hollow cylindrical glass tubing with nominal ID of 9 ± 1 μm (2000004 - TSP010150) and 20 ± 0.5 μm (2000008 - TSP020150) (56), both with an outer diameter of 150 μm, were obtained from Polymicro Technologies (Phoenix, AZ, USA). These fused silica fibers were cut into tubes 4.5 ± 0.5 cm in length, filled with water, and aligned along the z axis (or bore) of the magnet.

NMR diffusion measurements were performed using the PGSTE diffusion sequence (41) on a 9.4 T Bruker Avance NMR spectrometer equipped with a Bruker Micro5 system which produces gradients as large as 190 G/cm along each of three orthogonal directions (Bruker BioSpin GmbH, Rheinstetten, Germany). The following sequence parameters were used for the 20 μm ID tubes: $TR = 4.2$ s, $TE = 20$ ms, $\delta = 3$ ms, and $\Delta = 1000$ ms. Magnetic field gradients were applied along different directions with respect to the tube's axis from the $+z$ direction ($\theta = 0°$) to the $-z$ direction ($\theta = 180°$). The following angles were sampled: $\theta = 0°$, 45°, 68°, 79°, 85°, 88°, 90°, 92°, 95.6°, 101.3°, 112.5°, 135°, and 180°. For $\theta = 0°$, 45°, 67.5°, 112.5°, 135°, and 180°, G was increased from 0 to 45 G/cm in 16 equal increments and, for all other angles, G was increased from 0 to 160 G/cm in 32 equal increments. For $G_{max} = 160$ G/cm the resulting q_{max} and b_{max} were 1274 cm^{-1} and 7.32×10^7 s/cm^2, respectively. A series of experiments was performed with diffusion gradients applied along $\theta = 0°$ and 180°, and $\theta = 90°$ and 270° to assess the importance of background gradients in this system.

The following sequence parameters were used for the 9 μm ID tubes: $TR = 3.6$ s, $TE = 22$ ms, $\delta = 3$ ms, and $\Delta = 400$ ms. The following gradient directions were sampled: $\theta = 0°$, 45°, 79°, 85°, 88°, 90° and 180°. For $\theta = 0°$, 45° and 180°, G was increased from 0 to 45 G/cm in 16 equal increments, and for $\theta = 79°$, 85°, 88°, and 90°, G was increased from 0 to 160 G/cm in 32 equal steps. For $G_{max} = 160$ G/cm, the resulting q_{max} and b_{max} were 1911 cm^{-1} and 6.58×10^7 s/cm^2, respectively.

To study the effects of violating the short gradient pulse approximation, we used the following PGSTE sequence for 20 μm ID tubes with the following pairs of gradient duration, δ, and maximal gradient strength, G_{max}: $\delta = 2$ ms, $G_{max} = 160$ G/cm; $\delta = 4$ ms, $G_{max} = 80$ G/cm; $\delta = 8$ ms, $G_{max} = 40$ G/cm; $\delta = 16$ ms, $G_{max} = 20$ G/cm; $\delta = 32$ ms, $G_{max} = 10$ G/cm; $\delta = 64$ ms, $G_{max} = 5$ G/cm. For the 9 μm ID tubes the following parameters were used: $\delta = 3$ ms, $G_{max} = 160$ G/cm; $\delta = 6$ ms, $G_{max} = 80$ G/cm; $\delta = 12$ ms, $G_{max} = 40$ G/cm; $\delta = 24$ ms, $G_{max} = 20$ G/cm; $\delta = 48$ ms, $G_{max} = 10$ G/cm. In both cases, the diffusion gradients were applied perpendicular to the tubes' axis ($\theta = 90°$). The signal-to-noise ratios based on the signal in the absence of diffusion gradients were typically 10 000 and 5000 for the 20 and 9 μm ID tubes, respectively.

One potential artifact we have considered is the effect of polydispersity or variability in tube IDs (57) on the measured MR signal. The glass tubes are nominally 20 and 9 μm ID, but the manufacturer allows small deviations from these values in a pack of tubes. To assess the effect of the potential tube diameter heterogeneity on the signal attenuation, we propose the following expression:

$$E_\perp(\mathbf{q}_\perp, \Delta) = \frac{\int_0^\infty E_\perp(\mathbf{q}_\perp, \Delta, a)\, p(a)\, a^2\, da}{\int_0^\infty p(a)\, a^2\, da} \qquad (6)$$

where the total signal attenuation arising from restricted diffusion in the radial or transverse direction, $E_\perp(\mathbf{q}_\perp,\Delta)$, is the area-weighted average of such signals, $E_\perp(\mathbf{q}_\perp,\Delta,a)$, arising from a tube with radius a; $\rho(a)$ is the probability of a tube having a radius a. This expression weights the signal from each tube by its relative volume of spins. Eqn (6) is the cylindrical tube (two-dimensional) analog to a (3D) formula found in Packer and Rees (23) for the total signal caused by spherical pores with a known diameter distribution.

We have also considered the presence of variations in the cylinders' orientations. Let φ denote the angle between a cylinder and the z-axis. If $\rho(\varphi)$ is the probability density function for the tube orientations, then the MR signal attenuation when the diffusion gradients are applied along a direction perpendicular to the z-axis is given by

$$\begin{aligned} E(q,\Delta) &= \frac{\int_0^\pi E(q,\Delta,\varphi)\rho(\varphi)sin(\varphi)d\varphi}{\int_0^\pi \rho(\varphi)sin(\varphi)d\varphi} \\ &= \frac{\sum_{i=1}^{N} sin(\varphi_i)E_\perp(qcos(\varphi_i),\Delta)E_{//}(qsin(\varphi_i),\Delta)}{\sum_{i=1}^{N} sin(\varphi_i)} \end{aligned} \qquad (7)$$

where in the last step we assumed that there are a total of N tubes in the ensemble, where the orientation of the i^{th} tube is characterized by the angle φ_i. Note that the angle between the applied gradient and the i^{th} tube is $\pi/2 - \varphi_i$. This is the reason why the arguments of $E_\perp$ and $E_{//}$ are $qcos(\varphi_i)$ and $qsin(\varphi_i)$, respectively.

In all our simulations with finite gradient pulse duration, we used Callaghan's matrix product formalism (54), which represents a gradient pulse as a train of impulses (55). Our implementation for cylindrical pores was based on the description in Ref. (50), although several corrections in the formulas therein were necessary. In addition, our discretization scheme used the correction in Ref. (58), where the temporal spacing between separate impulses was taken to be 1 ms. Taking the dimensions of the matrices to be 33 was sufficient to produce accurate results. The bulk diffusivity value was computed using the first few points of the MR signal attenuation obtained when the diffusion gradients are applied parallel to the tubes' axis.

DOI: 10.1002/nbm

RESULTS

Figure 2 shows the PGSTE signal attenuation, $E_\perp(\mathbf{q}_\perp, \Delta)$, as a function of q value, $\mathbf{q}_\perp$, in the narrow and fat pulse regimes. In this study, gradients are oriented perpendicular to the tube wall (i.e. $\theta = 90°$). Figure 2a shows experimental and model data obtained for a pack of tubes with a nominal ID of 9 μm. Although the data are improved somewhat by the use of the matrix formalism – which takes into account the finite width of the gradient pulses – there is still some disagreement between the predicted and the experimental attenuation profiles when we assume the tube ID to be 9 μm. Figure 2b shows the same experimental data as in the previous panel now plotted against simulated data using different tube IDs. The best agreement is achieved when the diameter of the cylinders is chosen to be 8.2 μm for tubes that, according to the manufacturer, have a nominal ID of 9 ± 1 μm. Figure 2c shows signal attenuation vs q value data for a 20 μm ID pack; superimposed are simulated data using both narrow and fat pulses. Agreement between the experimental data and the finite pulse width or fat pulse simulations is excellent.

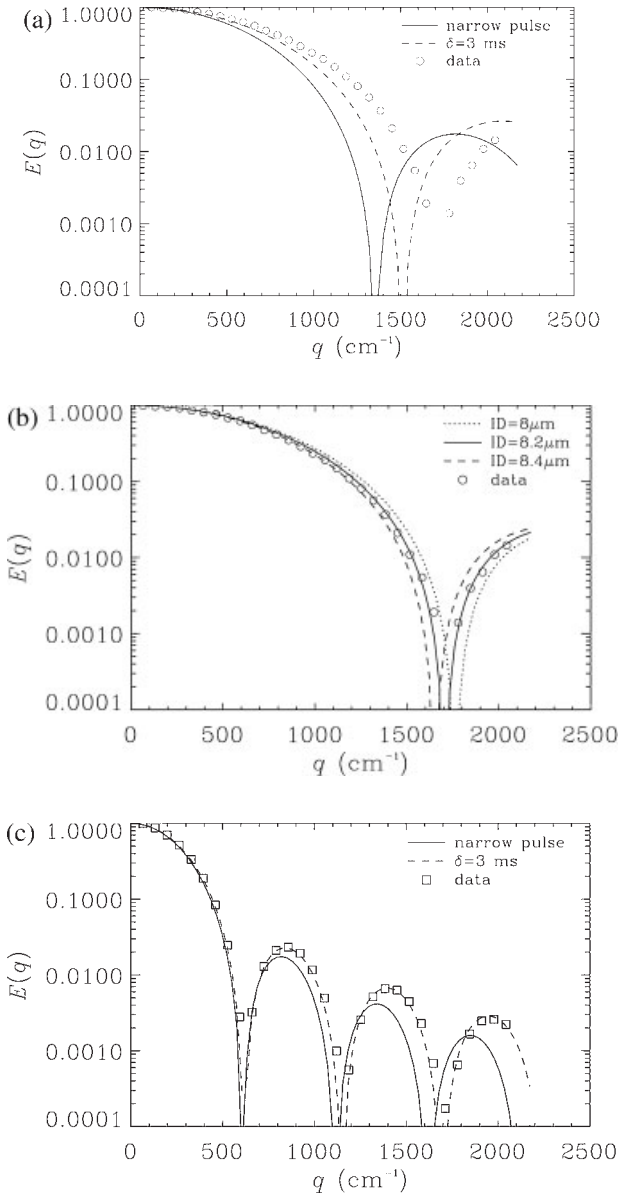

Figure 2. PGSTE signal attenuation, $E_\perp(\mathbf{q}_\perp, \Delta)$, as a function of q value, $\mathbf{q}_\perp$, in the narrow and fat pulse regimens. (a) Experimental data juxtaposed with simulations of signal attenuations for a 9 μm ID pack of tubes. Simulations using the narrow and fat pulse ($\delta = 3$ ms) are shown. (b) Same experimental data now plotted against simulation results for different tube IDs. (c) Signal attenuation vs q data for a 20 μm ID pack. The fat pulse simulations are in almost perfect agreement with experimental data.

Figure 3 shows $E_\perp(\mathbf{q}_\perp, \Delta)$ vs $\mathbf{q}_\perp$ data intended to study the effect of pulse duration, δ, on the signal attenuation profile. Simulations are performed using Callaghan's matrix operator framework with a correction in the discretization of the gradient pulses described in Ref. (58). Figure 3a shows experimental and simulated data for a nominal 9 μm ID pack of tubes for a range of pulse durations. The simulation performed in Fig. 3a assumes the tube ID to be 8.2 μm. Figures 3b,c show similar experimental data and model predictions for the 20 μm ID pack. Here again there is very good agreement between the experimental data and the simulations using a finite pulse width.

To assess the effect of the angle between the gradient direction and the cylinder axis, Fig. 4 provides experimental PGSTE data showing $E(\mathbf{q}, \Delta)$ vs $\mathbf{q}$ for different gradient orientations, θ. Superposed are simulated data obtained using Callaghan's matrix operator framework described above for $E_\perp(\mathbf{q}_\perp, \Delta)$, whereas $E_{//}(\mathbf{q}_{//})$ is calculated with the experimental pulse parameters using eqn (5). A tube ID of 8.2 μm is assumed in simulations in Fig. 4a and 20 μm in simulations in Fig. 4b. Agreement between the experimental and model data is excellent for all orientations.

Figure 5 examines the effect of polydispersity or variability of tube diameters in a cylindrical pack on the predicted $E_\perp(\mathbf{q}_\perp, \Delta)$ vs $\mathbf{q}_\perp$ profiles. Increasing the standard deviation of an assumed Gaussian diameter distribution [see technical specifications provided in Ref. (57)] smoothes the decay curve and introduces a slight horizontal shift in the diffraction minima. Simulations were performed using 5000 cylinders with Gaussian-distributed diameters with a mean ID of 9 μm.

Figure 6 examines the effect of variability in tube orientation on the predicted $E_\perp(\mathbf{q}_\perp, \Delta)$ vs $\mathbf{q}_\perp$ profiles within a pack of cylindrical tubes all with an assumed ID of 9 μm. Here, $\mathbf{q}_\perp$ is thought to be oriented perpendicular to the mean orientation of the cylinders. In our implementation, we started with 5000 angles normally distributed with zero mean, the standard deviation of which is denoted by σ_{ID}. Then the absolute values of these random angles were taken to be φ_i ($i = 1,2,\ldots, 5000$) and used in the evaluation of eqn (7). Increasing the standard deviation of the Gaussian orientation distribution attenuates

DOI: 10.1002/nbm

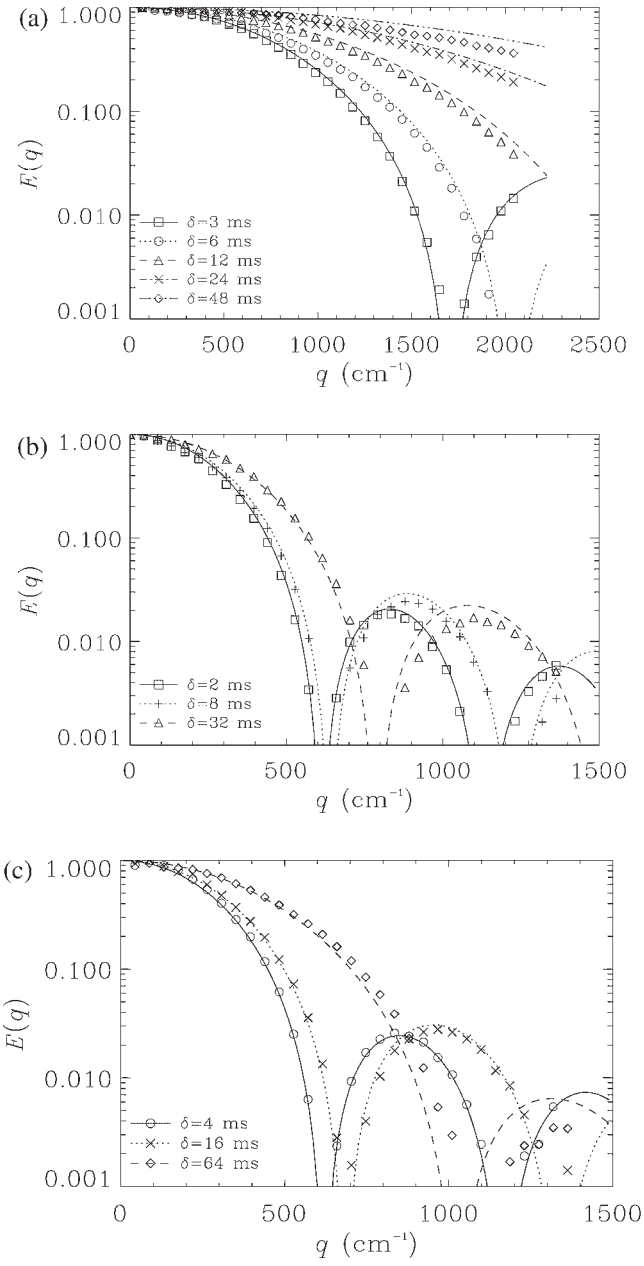

Figure 3. PGSTE $E_{\perp}(\mathbf{q}_{\perp},\Delta)$ vs $\mathbf{q}_{\perp}$ data for various pulse durations, δ. (a) Experimental data obtained for the nominal 9 μm ID pack of tubes along with simulations performed by setting the ID to 8.2 μm. (b,c) Experimental data and simulation results for 20 μm ID tubes. The data from 20 μm ID tubes are separated into two panels for clarity.

the decay; however, it does not appear to produce a shift in q values at which the diffraction minima occur.

DISCUSSION

Figure 4 shows the strong effect of gradient orientation, θ, on signal attenuation, $E(\mathbf{q},\Delta)$, previously reported in Ref. (39). When the gradient direction is normal (i.e. $\theta = 90^{\circ}$) or nearly normal to the tube's axis, the familiar diffraction peaks reported in Callaghan *et al*. (20), are observed.

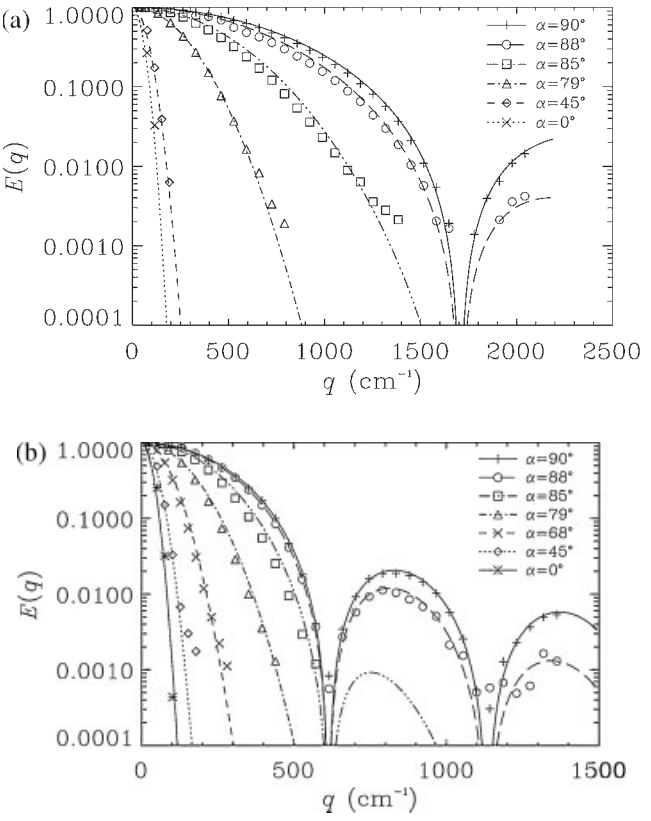

Figure 4. $E(\mathbf{q},\Delta)$ vs $\mathbf{q}$ experimental PGSTE data for different gradient orientations, α. Superimposed are simulated data obtained using the matrix operator framework. A tube ID of 8.2 μm is assumed in (a); 20 μm in (b). Excellent agreement is seen between the experimental data and the model.

However, for small angular deviations from $\theta = 90^{\circ}$, these diffraction peaks virtually disappear, and the signal decay appears Gaussian (39).

This strong angular dependence of $E(\mathbf{q},\Delta)$on gradient orientation can now be understood in a physically intuitive way by considering the form of eqn (3) above. The net signal attenuation, $E(\mathbf{q},\Delta)$, results from the product of signal attenuations arising from the 'free' (axial) and 'restricted' (radial) diffusion processes. The free diffusion signal decays rapidly with increasing $\mathbf{q}$, particularly in water, in which the diffusion coefficient is high. The restricted diffusion signal decays slowly with $\mathbf{q}$, because spins trapped in the tubes experience comparatively little dephasing owing to their tight geometric confinement. Close to $\theta = 90^{\circ}$, there is negligible signal attenuation from 'free diffusion' ($E_{//}(\mathbf{q}_{//}) \cong 1$) so that $E(\mathbf{q},\Delta) \cong E_{\perp}(\mathbf{q}_{\perp},\Delta)$, i.e. the net signal decay is almost exclusively determined by the slowly decaying, oscillating signal arising from the restricted diffusion process. However, as θ deviates slightly from 90°, the negative exponent in eqn (5) grows rapidly, so that $E_{//}(\mathbf{q}_{//})$ falls quickly with $\mathbf{q}$. The low-$\mathbf{q}$ behavior of the net signal, $E(\mathbf{q},\Delta)$, then becomes dominated by $E_{//}(\mathbf{q}_{//})$. Thus, only when the diffusion gradient is applied perpendicular or

DOI: 10.1002/nbm

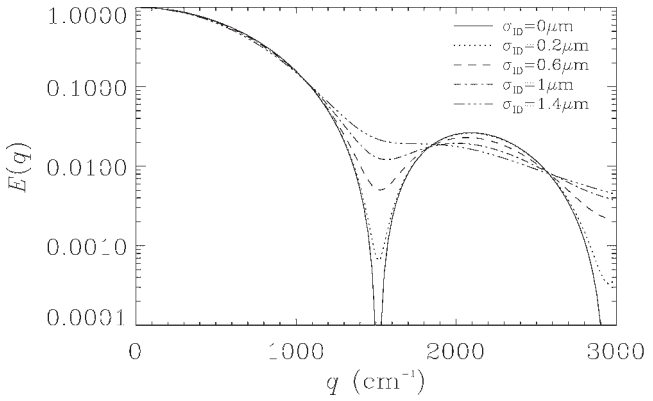

Figure 5. Simulations examining the effect of differences in the variance of the diameter distribution of a cylindrical pack of tubes on the predicted $E_{\perp}(\mathbf{q}_{\perp},\Delta)$ vs $\mathbf{q}_{\perp}$ curves. Increasing the variance of an assumed Gaussian distribution of tube diameters affects both the **q** values at which minima are predicted and the sharpness and depth of these minima

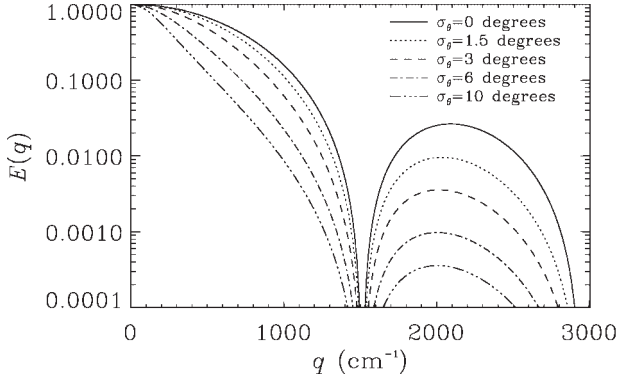

Figure 6. Superposition of the 3D model of diffusion in tubes to describe the behavior of $E_{\perp}(\mathbf{q}_{\perp},\Delta)$ in a pack of cylinders with different degrees of splay of their axial director or orientation vector. Increasing the variance of an assumed Gaussian distribution of splay angles around a mean angle of zero decreases the sharpness and depth of the diffraction minima observed in the $E_{\perp}(\mathbf{q}_{\perp},\Delta)$ profile.

nearly perpendicular to the tubes' axis are the effects of restricted diffusion observed. Otherwise, the diffusion process appears to be Gaussian or free. Please note that, if these tubes were filled with a medium (e.g. a solvent, polymeric solution, or gel) with diffusivity that is several orders of magnitude smaller than that of water, we would expect this strong angular dependence on $E(\mathbf{q},\Delta)$ to be less pronounced.

We can rule out the possibility that the dependence of $E(\mathbf{q})$ on gradient orientation, originally observed by Avram *et al*. (39), arises from gradients caused by differences in magnetic susceptibility between the walls of the fused silica tubes and the bathing aqueous fluid. Because the tubes' axes are aligned with the main (static) magnetic field, the theoretical analysis and experiments of Callaghan (59) demonstrate that any induced magnetic field within the tubes must be uniform, i.e. no susceptibility gradients are generated within the water in the tube or at the water–tube interface, a fact long known to NMR spectroscopists. Susceptibility gradients caused by applying the diffusion gradients are expected to be negligible. The series of experiments performed with diffusion gradients applied along $\theta = 0^{\circ}$ and 180°, and $\theta = 90^{\circ}$ and 270° showed that background gradients are negligible.

Using the notion of statistical independence of the average propagators, we can begin to assemble more complex models of solvent diffusion within complicated 3D porous or cellular structures. Obvious examples are the two cases of polydispersity in tube diameter and tube orientation presented above. However, diffusion is easily modeled in an array of rectangular prisms having arbitrary aspect ratios and orientations with respect to the laboratory coordinate frame. Models of cylindrical tubes capped at each end by impermeable plates with arbitrary aspect ratios can also be constructed using the reasoning employed above to arrive at eqn (3). A case in point is the article by Söderman and Jönsson (27), which presents a formula for the signal attenuation profile, $E(\mathbf{q},\Delta)$, in a right cylindrical tube of radius R with end caps spaced a distance L apart. It is not possible to discern from the complicated formulae for $E(\mathbf{q},\Delta)$ given in their eqns (3–4), that an equivalent, simple and intuitive expression for $E(\mathbf{q},\Delta)$ can be obtained by multiplying $E_{\perp}(\mathbf{q}_{\perp},\Delta)$ given by Callaghan (18) for a restricted cylinder of radius R, and $E_{//}(\mathbf{q}_{//})$ given by Tanner and Stejskal (60) for a pair of infinite impermeable parallel plates spaced a distance L apart, the surface normals of which coincide with the cylinder's axis. This simple result follows directly from our eqn (3) and illustrates the power of this approach.

If we further assume that these restricted compartments are non-communicating or non-exchanging, we can use eqn (3) to create composite models of complex closed-cell porous media with inclusions or pores with different sizes, shapes, and orientations, simply by superposing the MR signals produced by each pore weighted by the pore volume. This approach should be useful in building more realistic models of heterogeneous porous media, such as lung tissue, closed-cell foams, zeolites, and arrays of plant cells.

In biomedical research and medical imaging applications, improved models of hindered and restricted diffusion in brain white matter, such as CHARMED, are advancing our understanding of normal and abnormal development as well as the diagnosis and management of numerous neurological diseases (11) and even psychiatric disorders. Moreover, the determination of nerve fiber orientation *in vivo* in brain white matter has allowed radiologists and neuroscientists to visualize brain white matter structure. One such embodiment is in computing trajectories of white matter fascicles in the brain and in

DOI: 10.1002/nbm

cardiac muscle in the heart, for which we coined the term DTI fiber 'tractography' (61). An improvement in our ability to determine nerve fascicle orientation more accurately and precisely, which exploits the orientational sensitivity that we have observed in impermeable tubes and in white matter using CHARMED MR, may further advance our ability to track nerve fascicles in the central and peripheral nervous systems.

Different types of polydispersity have different effects on the $E(\mathbf{q},\Delta)$ profile. Increased variability in tube diameters has the primary effect of making $E(\mathbf{q},\Delta)$ broader and shallower and secondarily shifting the minima to higher q values. Variability in fiber orientation only attenuates the signal when $\theta = 90^\circ$ without shifting the diffraction minima to higher or lower q values. We expect to be able to exploit these distinct effects on the attenuation profile to infer the variability in tube diameter and tube orientation. Furthermore, the disappearance of diffraction minima in packs of tubes with a modest range of fiber diameters may help to explain why diffraction minima have not been observed in packs of myocytes or nerve axons, which generally do not have a sharp (or δ-function-like) diameter distribution [as discussed in Ref. (62)].

When using eqn (6), we have assumed particular diameter distributions for a pack of tubes. However, we can also invert eqn (6) to infer or estimate the diameter distribution of a pack of tubes experimentally from their signal attenuation profiles, even when the diameter distribution is not known *a priori*. This idea has already been applied in the porous media field to measure the diameter distribution in emulsions (23), and has recently been applied to measure the diameter distribution within a pack of nerve axons using an extension of the CHARMED MRI framework that we call *AxCaliber* (63,64), the goal of which is to estimate, among other microstructural parameters, the axon radius distribution, $p(a)$, that appears in eqn (6) above.

Finally, on the basis of our findings here, both the CHARMED and *AxCaliber* MRI frameworks can now be made more accurate by incorporating Callaghan's robust matrix operator method for predicting the diffusion-weighted data acquired using sequences with 'fat pulses'. This is because MR scanners currently used in clinical or biological settings are limited in their ability to produce strong, narrow diffusion gradient pulses so their sequences seldom satisfy the narrow pulse approximation. However, this matrix operator method should permit us to deconvolve the effect of fat pulses, correcting for the motional narrowing they cause when estimating of pore geometry.

CONCLUSIONS

The 3D model of restricted diffusion within a pack of cylindrical tubes fits the experimental MR signal vs $\mathbf{q}$ data with great fidelity. It not only predicts the strong angular or θ-dependence of the MR signal, but also predicts its dependence on the diffusion pulse gradient duration, δ. We had already observed enhanced angular sensitivity of the restricted tube component in the CHARMED MR of optic nerve and spinal cord, but the analysis provided above explains the origin of this high angular resolution in a physically intuitive manner. Exquisite sensitivity to tube wall orientation should also improve the accuracy and precision of fiber 'tractography' results in coherently organized white matter fascicles beyond that provided by conventional DTI. This increased angular resolution arises from the exquisite angular sensitivity provided by the restricted 'intra-axonal' compartment in this model. The ability to combine different models of restricted diffusion (e.g. plates and cylinders) opens up the possibility for building complex models of diffusion in cells, rocks, closed-cell foams, etc. from component elements. Finally, the experimental model system used here provides convincing experimental validation of the assumptions used to construct the restricted diffusion contribution to the CHARMED MRI framework, which is based on the statistical independence of the net displacements along the axial and radial directions in cylindrical tubes.

Acknowledgements

The Intramural Research Program of the Eunice Kennedy Shtriver National Institute of Child Health and Human Development (NICHD) supported P.J.B. and E.O; L.A., A.B.-S. and Y.C. were all supported, in part, by the Israel–US Bi-National Science Foundation (BSF). We thank Liz Salak for her careful editing of this manuscript. Raisa Freidlin helped prepare several figures.

REFERENCES

1. DeGennes PG. *Scaling Concepts in Polymer Physics*. Cornell University Press: Ithaca, NY, 1976.
2. Kimmich R, Bachus R. NMR field-cycling relaxation spectroscopy, transverse NMR relaxation, self-diffusion and zero-shear viscosity: defect diffusion and reptation in non-glassy amorphous polymers. *Colloid Polym. Sci.* 1982; **260**(10): 911–936.
3. Davis ME. Ordered porous materials for emerging applications. *Nature* 2002; **417**: 813–821.
4. Hubbell JA. Biomaterials in tissue engineering. *Nat Biotechnol* 1995; **13**: 565–576.
5. King MD, Houseman J, Roussel SA, van Bruggen N, Williams SR, Gadian DG. q-Space imaging of the brain. *Magn Reson Med* 1994; **32**(6): 707–713.
6. King MD, Houseman J, Gadian DG, Connelly A. Localized q-space imaging of the mouse brain. *Magn Reson Med* 1997; **38**(6): 930–937.
7. Nossin-Manor R, Duvdevani R, Cohen Y. Effect of experimental parameters on high b-value q-space MR images of excised rat spinal cord. *Magn Reson Med* 2005; **54**(1): 96–104.

DOI: 10.1002/nbm

8. Assaf Y, Mayk A, Cohen Y. Displacement imaging of spinal cord using q-space diffusion-weighted MRI. *Magn Reson Med* 2000; **44**(5): 713–722.
9. Assaf Y, Ben-Bashat D, Chapman J, Peled S, Biton IE, Kafri M, Segev Y, Hendler T, Korczyn AD, Graif M, Cohen Y. High b-value q-space analyzed diffusion-weighted MRI: application to multiple sclerosis. *Magn Reson Med* 2002; **47**(1): 115–126.
10. Biton IE, Mayk A, Kidron D, Assaf Y, Cohen Y. Improved detectability of experimental allergic encephalomyelitis in excised swine spinal cords by high b-value q-space DWI. *Exp Neurol* 2005; **195**(2): 437–446.
11. Cohen Y, Assaf Y. High b-value q-space analyzed diffusion-weighted MRS and MRI in neuronal tissues: a technical review. *NMR Biomed* 2002; **15**(7–8): 516–542.
12. Tanner JE. Self-diffusion of water in frog muscle. *Biophys J* 1979; **28**(1): 107–116.
13. Kim S, Chi-Fishman G, Barnett AS, Pierpaoli C. Dependence on diffusion time of apparent diffusion tensor of *ex vivo* calf tongue and heart. *Magn Reson Med* 2005; **54**(6): 1387–1396.
14. Mair RW, Hrovat MI, Patz S, Rosen MS, Ruset IC, Topulos GP, Tsai LL, Butler JP, Hersman FW, Walsworth RL. ^{3}He lung imaging in an open access, very-low-field human magnetic resonance imaging system. *Magn Reson Med* 2005; **53**(4): 745–749.
15. van As H, Palstra W, Tallarek U, van Dusschoten D. Flow and transport studies in (non)consolidated porous (bio)systems consisting of solid or porous beads by PFG NMR. *Magn Reson Imaging* 1998; **16**(5–6): 569–573.
16. Kuchel PW, Coy A, Stilbs P. NMR ''diffusion-diffraction'' of water revealing alignment of erythrocytes in a magnetic field and their dimensions and membrane transport characteristics. *Magn Reson Med* 1997; **37**(5): 637–643.
17. Hills BP, Snaar JEM. Dynamic q space microscopy of cellular tissue. *Mol Phys* 1992; **76**(4): 979–994.
18. Callaghan PT. *Principles of Nuclear Magnetic Resonance Microscopy.* Oxford University Press: Oxford, 1991.
19. Callaghan PT, Eccles CD, Xia Y. NMR microscopy of dynamic displacements: k-space and q-space imaging. *J. Phys. E: Sci. Instrum.* 1988; **21**: 820–822.
20. Callaghan PT, Coy A, Macgowan D, Packer KJ, Zelaya FO. Diffraction-like effects in NMR diffusion studies of fluids in porous solids. *Nature* 1991; **351**: 467.
21. Mair RW, Wong GP, Hoffmann D, Hurlimann MD, Patz S, Schwartz LM, Walsworth RL. Probing porous media with gas diffusion NMR. *Phys Rev Lett* 1999; **83**(16): 3324–3327.
22. Sen PN, Schwartz LM, Mitra PP. Probing the structure of porous media using NMR spin echoes. *Magn Reson Imaging* 1994; **12**(2): 227–230.
23. Packer KJ, Rees C. Pulsed NMR studies of restricted diffusion. 1. Droplet size distributions in emulsions. *J. Colloid Interface Sci.* 1972; **40**(2): 206–218.
24. Cory DG, Garroway AN. Measurement of translational displacement probabilities by NMR: an indicator of compartmentation. *Magn Reson Med* 1990; **14**(3): 435–444.
25. Komlosh ME, Callaghan PT. Segmental motion of entangled random coil polymers studied by pulsed gradient spin echo nuclear magnetic resonance. *J. Chem Phys* 1998; **109**(22): 10053–10067.
26. Boss BD, Stejskal EO. Anisotropic diffusion in hydrated vermiculite. *J. Chem. Phys.* 1965; **43**: 1068–1069.
27. Söderman O, Jönsson B. Restricted diffusion in cylindrical geometry. *J. Magn. Reson. Ser. A* 1995; **117**(1): 94–97.
28. Assaf Y, Basser PJ. Composite hindered and restricted model of diffusion (CHARMED) MR imaging of the human brain. *Neuroimage* 2005; **27**(1): 48–58.
29. Assaf Y, Freidlin RZ, Rohde GK, Basser PJ. New modeling and experimental framework to characterize hindered and restricted water diffusion in brain white matter. *Magn Reson Med* 2004; **52**(5): 965–978.
30. Stejskal EO. Use of spin echoes in a pulsed magnetic-field gradient to study restricted diffusion and flow. *J. Chem Phys* 1965; **43**(10): 3597–3603.
31. Brownstein KR, Tarr CE. Importance of classical diffusion in NMR studies of water in biological cells. *Phys. Rev. A.* 1979; **19**(6): 2446–2453.
32. Callaghan PT, Coy A. PGSE NMR and molecular translational motion in porous media. In *NMR probes of molecular dynamics*, Tycko R (ed). 1994; 489–523.
33. Mitra PP, Sen PN, Schwartz LM, Le Doussal P. Diffusion propagator as a probe of the structure of porous media. *Phys Rev Lett* 1992; **68**(24): 3555–3558.
34. Mitra PP, Sen PN. Effects of microgeometry and surface relaxation on NMR pulsed-field-gradient experiments: simple pore geometries. *Phys Rev. B. Condensed Matter* 1992; **45**(1): 143–156.
35. Basser PJ, Mattiello J, Le Bihan D. MR diffusion tensor spectroscopy and imaging. *Biophys. J.* 1994; **66**(1): 259–267.
36. Pierpaoli C, Jezzard P, Basser PJ, Barnett A, Di Chiro G. Diffusion tensor MR imaging of the human brain. *Radiology* 1996; **201**(3): 637–648.
37. Crank J. *The Mathematics of Diffusion*. Clarendon Press: Oxford, 1956.
38. Kärger J, Heink W. The propagator representation of molecular-transport in microporous crystallites. *J Magn Reson* 1983; **51**(1): 1–7.
39. Avram L, Assaf Y, Cohen Y. The effect of rotational angle and experimental parameters on the diffraction patterns and micro-structural information obtained from q-space diffusion NMR: implication for diffusion in white matter fibers. *J Magn Reson* 2004; **169**(1): 30–38.
40. Avram L, Assaf Y, Basser PJ, Cohen Y. 2005; Finer discrimination of fiber orientation at high q diffusion MR: theoretical and experimental confirmation. In 13th Annual ISMRM, Miami, FL. 219.
41. Tanner JE. Use of the stimulated echo in NMR diffusion studies. *J Chem Phys* 1970; **52**(5): 2523–2526.
42. Hahn EL. *Spin-echoes. Phys. Rev.* 1950; **80**(4): 580–594.
43. Carr HY, Purcell EM. Effects of diffusion on free precession in nuclear magnetic resonance experiments. *Phys. Rev.* 1954; **94**(3): 630–638.
44. Stejskal EO, Tanner JE. Spin diffusion measurements: spin echoes in the presence of time-dependent field gradient. *J Chem Phys* 1965; **42**(1): 288–292.
45. Kärger J, Pfeifer H, Heink W. Principles and applications of self-diffusion measurements by nuclear magnetic resonance. In *Advances in Magnetic Resonance*, Waugh J (ed). Academic Press: New York, 1988; 1–89.
46. Crank J. *The Mathematics of Diffusion*. Oxford University Press: Oxford, 1975.
47. Carslaw HS, Jaeger JC. *Conduction of Heat in Solids*. Oxford University Press: Oxford, 1959.
48. Robertson B. Spin-echo decay of spins diffusing in a bounded region. *Phys. Rev.* 1966; **151**(1): 273–277.
49. Neuman CH. Spin echo of spins diffusing in a bounded medium. *J. Chem. Phys.* 1974; **60**(11): 4508–4511.
50. Codd SL, Callaghan PT. Spin echo analysis of restricted diffusion under generalized gradient waveforms: planar, cylindrical, and spherical pores with wall relaxivity. *J Magn Reson* 1999; **137**(2): 358–372.
51. Callaghan PT. Pulsed-gradient spin-echo NMR for planar, cylindrical, and spherical pores under conditions of wall relaxation. *J Magn Reson Ser A* 1995; **113**(1): 53–59.
52. van Gelderen P, DesPres D, van Zijl PC, Moonen CT. Evaluation of restricted diffusion in cylinders. Phosphocreatine in rabbit leg muscle. *J Magn Reson B* 1994; **103**(3): 255–260.
53. Callaghan PT, Stepisnik J. Generalized analysis of motion using magnetic field gradients. *Advances in Magnetic Resonance* 1996; **19**: 325–388.
54. Callaghan PT. A simple matrix formalism for spin echo analysis of restricted diffusion under generalized gradient waveforms. *J Magn Reson* 1997; **129**(1): 74–84.
55. Caprihan A, Wang LZ, Fukushima E. A multiple-narrow-pulse approximation for restricted diffusion in a time-varying field gradient. *J. Magn. Reson. A* 1996; **118**: 94–102.
56. Macomber J, Nico P, Nelson G. Internal diameter measurement of small capillary tubing. 2003. June.http://www.polymicro.com/tech/applicationnotes/appnote_2003JUN.htm
57. Macomber J, Nico P, Nelson G. Dimensional study of capillary tubing used for gas chromatography. 2004. June.http://www.polymicro.com/tech/applicationnotes/appnote_2004JUN.htm

DOI: 10.1002/nbm

58. Özarslan E, Basser PJ. MR diffusion-''diffraction'' phenomenon in multi-pulse-field-gradient experiments. *J Magn Reson* 2007; **188**(2): 285–294.
59. Callaghan PT. Susceptibility-limited resolution in nuclear-magnetic-resonance microscopy. *J Magn Reson* 1990; **87**(2): 304–318.
60. Tanner JE, Stejskal EO. Restricted self-diffusion of protons in colloidal systems by the pulsed-gradient, spin-echo method. *J Chem Phys* 1968; **49**(4): 1768–1777.
61. Basser PJ, Pajevic S, Pierpaoli C, Duda J, Aldroubi A. *In vivo* fiber-tractography in human brain using diffusion tensor MRI (DT-MRI) data. *Magn. Reson. Med.* 2000; **44**(4): 625–632.
62. Peled S, Cory DG, Raymond SA, Kirschner DA, Jolesz FA. Water diffusion, T(2), and compartmentation in frog sciatic nerve. *Magn Reson Med* 1999; **42**(5): 911–918.
63. Assaf Y, Freidlin RZ, Basser PJ. 2005; The measurement of the axon diameter distribution in white matter using diffusion MR methods. In 13th Annual ISMRM, Miami, FL. 842.
64. Assaf Y, Blumenfeld-Katzir T, Yovel Y, Basser PJ. AxCaliber: a method for measuring axon diameter distribution from diffusion magnetic resonance imaging. *Magn. Reson. Med.* 2008; **59**(6), 1347–1354.

DOI: 10.1002/nbm